# "2x2 MIMO FBMC-OQAM Signal Transmission over a Seamless Fiber–Wireless System in W-band"

Rottenberg, François ; Dat, Pham Tien ; Kanno, Atsuhi ;
Horlin, François ; Louveaux, Jérôme ; Yamamoto, Naokastu

**Abstract**

Offset-QAM-based filterbank multicarrier (FBMC-OQAM) is an attractive modulation candidate to increase the spectral efficiency of radio-over-fiber and fiber--wireless systems. In this paper, we first propose a general framework for MIMO FBMC-OQAM transmission systems, including the description of algorithms for mitigation of the channel impairments. The proposed design is scalable in the number of transmitted streams and flexible as multiple asynchronous users can be accommodated. The proposed system is experimentally validated in a 2x2 MIMO FBMC-OQAM signal over a seamless fiber--wireless in the W-band for the first time. Satisfactory performance is confirmed for a data rate of up to 18 Gb/s in both downlink and uplink directions. Furthermore, algorithms previously proposed by the authors for channel estimation and phase noise compensation are experimentally validated, confirming their effectiveness. Finally, we show that, for a similar error vector magnitude performance, an FBMC-OQ...

Document type : *Article de périodique (Journal article)*

# 2x2 MIMO FBMC-OQAM Signal Transmission over a Seamless Fiber–Wireless System in W-band

**François Rottenberg[1,2], Pham Tien Dat[3], Trung-Hien Nguyen[2], Atsushi Kanno[3], François Horlin[2], Jérôme Louveaux[1], Naokatsu Yamamoto[3]**

[1] *ICTEAM institute, Université catholique de Louvain, 1348 Louvain-la-Neuve, Belgium*
[2] *OPERA department, Université libre de Bruxelles, 1050 Brussels, Belgium*
[3] *National Institute of Information and Communications Technology, Tokyo 184-8795, Japan*

*DOI: XX.YYYY/JPHOT.2017.XXXXXXX*
*XXXX-YYYY/$25.00 ©2017 IEEE*

Manuscript received Month Day, 2017; revised Month Day, 2017. First published Month Day, 2017. Current version published Month Day, 2017. This work was supported as a part of the "Research and development for expansion of radiowave resources", supported by the Ministry of Internal Affairs and Communications, Japan, and the "Fonds pour la Formation a la Recherche dans l'Industrie et dans l'Agriculture".
Corresponding author: F. Rottenberg (e-mail: francois.rottenberg@uclouvain.be), P. T. Dat (e-mail: ptdat@nict.go.jp).

**Abstract:**
Offset-QAM-based filterbank multicarrier (FBMC-OQAM) is an attractive modulation candidate to increase the spectral efficiency of radio-over-fiber and fiber–wireless systems. In this paper, we first propose a general framework for MIMO FBMC-OQAM transmission systems, including the description of algorithms for mitigation of the channel impairments. The proposed design is scalable in the number of transmitted streams and flexible as multiple asynchronous users can be accommodated. The proposed system is experimentally validated in a 2x2 MIMO FBMC-OQAM signal over a seamless fiber–wireless in the W-band for the first time. Satisfactory performance is confirmed for a data rate of up to 18 Gb/s in both downlink and uplink directions. Furthermore, algorithms previously proposed by the authors for channel estimation and phase noise compensation are experimentally validated, confirming their effectiveness. Finally, we show that, for a similar error vector magnitude performance, an FBMC-OQAM system can achieve a 25% higher throughput rate than a corresponding orthogonal frequency division multiplexing-based fiber–wireless system.

**Index Terms:**
Fiber–wireless convergence, radio-over-fiber, FBMC-OQAM, MIMO.

## 1. Introduction

The fifth generation of mobile communication systems (5G) is expected to offer a huge increase in the network capacity. In these networks, radio-over-fiber (RoF) systems would be very useful for mobile fronthaul transmission to reduce the required data rate, transmission latency, and simplify remote antenna sites [1]–[3]. Seamless fiber–wireless systems in high-frequency bands based on RoF technology would also be very attractive for flexible and resilient broadband access networks where the use of fiber cables is not always possible. RoF and fiber–wireless systems using cyclic prefix-orthogonal frequency division multiplexing (CP-OFDM) have already been studied in many works [4], [5]. CP-OFDM has the main advantages of a relatively low complexity of implementation based on the Fast Fourier transform (FFT) and simple channel compensation at the receiver. Extension to multiple-input multiple-output (MIMO) scenarios is also straightforward thanks to the orthogonality ensured in the complex domain. However, the rectangular pulse shaping of the FFT

filters induces high spectral leakage. This results in the need of large guard bands at the edges of the system band to prevent out-of-band emission. Furthermore, the cyclic prefix (CP), which is introduced in order to simplify the equalization of the channel at the receiver, induces an additional loss of spectral efficiency.

In the light of these limitations, the offset-QAM-based filter-bank multicarrier (FBMC-OQAM) modulation has been regarded as an attractive alternative [6]. This modulation uses a pulse shape, which is more spread out in time and is much more spectrally contained. As a result, very small guard bands are sufficient at the edges of the spectrum, resulting in a higher spectral efficiency. Furthermore, it does not require a CP, which again increases the spectral efficiency. Recently, the FBMC-OQAM modulation has been considered in some works for RoF and seamless fiber–wireless systems. The authors in [7] proposed and demonstrated a centralized pre-equalization algorithm to compensate for the channel impairments. In [8], full-duplex quasi-gapless carrier aggregation is demonstrated, taking advantage of the very high spectral containment of FBMC. In [9], a simultaneous transmission of OFDM and FBMC signals is experimentally demonstrated. In [10], [11], the authors respectively propose a 2x2 and a 4x4 MIMO FBMC-OQAM transmission over a radio-over-multicore fiber system and wireless links in the 2-GHz band.

In this paper, we first propose a general system design for MIMO FBMC-OQAM systems. We design a frame structure which is compliant with the FBMC-OQAM modulation and allows for efficient synchronization and channel estimation. The frame structure is scalable with the number of antennas and is capable of handling asynchronous uplink user transmission. The proposed transceiver design is then experimentally validated in a 2x2 MIMO FBMC-OQAM signal over a seamless fiber–wireless in the W-band in both downlink (DL) and uplink (UL) directions. To realize the seamless fiber–wireless system, we use analog RoF technology. At remote antenna units (RAUs), received optical signals are converted directly to radio signals using an optical-to-electrical converter, without going through any modulation format and waveform change. Using this technology, the signal waveform and modulation format are maintained in the whole transmission system. In addition, to realize a high spectral efficient transmission for MIMO wireless signals in the high frequency band, wavelength-division multiplexing (WDM) intermediate frequency-over-fiber (IFoF) systems with an electrical signal up-conversion to the W-band at RAUs are used. The proposed system is scalable for large-scale MIMO fiber–wireless systems and is different from previous works in [10], [11] where the authors used a multicore fiber to multiplex the streams on the optical fiber instead of WDM and where the wireless link was in the 2-GHz band instead of the W-band. Moreover, using a larger bandwidth, we achieve a data rate of up to 18 Gb/s compared to the rates of 4.42 Gb/s and 11.04 Gb/s demonstrated in [10] and [11] respectively.

In addition, we demonstrate that the time domain (TD) channel estimation algorithm proposed in [12] can provide high performance gain with respect to conventional approaches in the frequency domain (FD). We also observed that the transmitted signals are affected by the random phase variations of local oscillators (LOs) used for the signal up-conversion to the W-band at the RAU, even when the LOs are synchronized by 10-MHz output and input ports. This happens when multiple LO signal sources, which are necessary for scalable and large-scale MIMO fiber–wireless systems, are used for the signal up-conversion at RAUs, and envelope detections are used for signal down-conversion at the remote radio heads (RRHs). To compensate for the phase noise (PN) effects, we adopt the blind PN estimator devised in [13]. The proposed frame structure does not require the periodic transmission of pilot symbols so that the system achieves a maximal spectral efficiency. To the best of the authors knowledge, it is the first time that a MIMO FBMC-OQAM seamless fiber–wireless system in the W-band is experimentally investigated in both DL and UL directions.

The rest of this paper is structured as follows. Section 2 presents a general transceiver design for MIMO FBMC-OQAM systems. Section 3 presents the experimental setup for MIMO signal transmission in both DL and UL directions, used to validate the proposed transceiver design. Section 4 provides the experimental results. Finally, Section 5 concludes the paper.

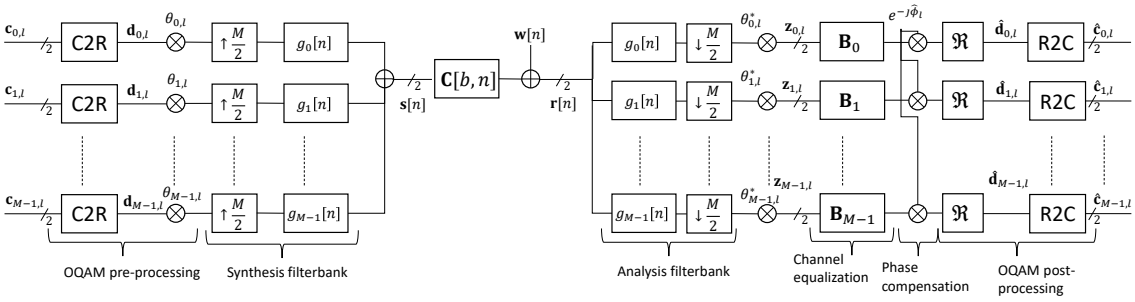


Fig. 1. Equivalent MIMO Offset-QAM-based filterbank multicarrier transceiver chain.

***Notations***

Vectors and matrices are denoted by bold lowercase and uppercase letters, respectively (resp.). Superscripts $^*$, $^T$ and $^H$ stand for conjugate, transpose and Hermitian transpose operators. The symbols $\Im$ and $\Re$ denote the imaginary and real parts, respectively. $\jmath$ is the imaginary unit.

## 2. Transceiver Design for MIMO FBMC-OQAM Systems

An equivalent block diagram of the system under consideration is shown in Fig. 1, holding both for UL and DL directions. We respectively denote by $M$ and $N_s$ the number of subcarriers and the number of complex symbols transmitted on each subcarrier. The set of active subcarriers is denoted by $\mathcal{M}$. The number of transmitted streams is equal to $S$ and we assume $S$ transmit and receive antennas. The subscripts $m$ and $l$ respectively refer to the subcarrier and multicarrier symbol indexes. At the transmitter, the complex symbols $\mathbf{c}_{m,l} \in \mathbb{C}^{S\times 1}$ coming at rate $1/T$ are first converted to the real symbols $\mathbf{d}_{m,l} \in \mathbb{R}^{S\times 1}$ at the twice faster rate $2/T$. The real symbols $\mathbf{d}_{m,l}$ are alternatively made of the real and imaginary parts of the symbols $\mathbf{c}_{m,l}$. Note that $\mathbf{c}_{m,l}$ and $\mathbf{d}_{m,l}$ are two-dimensional vectors containing on each row one stream of information. The symbols $\mathbf{d}_{m,l}$ are first multiplied by $\theta_{m,l} = \jmath^{m+l}$ to obtain the OQAM real-imaginary pattern before being processed by the synthesis filterbank (SFB). At the SFB, the symbols on each subcarrier are first upsampled by a factor $M/2$ before being filtered and re-combined. The transmit baseband equivalent signal, denoted by $\mathbf{s}[n]$ at rate $1/T_s = M/T$ can be written as

$$\mathbf{s}[n] = \sum_{l=0}^{2N_s-1} \sum_{m\in\mathcal{M}} \mathbf{d}_{m,l}\theta_{m,l} g_m[n - l\frac{M}{2}],$$

where $g_m[n] = g[n]e^{\jmath\frac{2\pi m}{M}(n-\frac{M\kappa-1}{2})}$. The phase term $\frac{L_g-1}{2}$ is inserted in order to have a causal filter $g_{m,l}[n]$ [14]. The real pulse $g[n]$ is chosen to be the Phydyas prototype filter [15] which is of length $M\kappa$, where $\kappa$ is the so-called overlapping factor. The received signal $\mathbf{r}[n]$ is processed by the analysis filterbank (AFB). The symbols after the AFB and OQAM compensation are given by

$$\mathbf{z}_{m,l} = \theta^*_{m,l} \sum_{n=0}^{M\kappa-1} \mathbf{r}[n] g^*_m[n - l\frac{M}{2}]. \tag{1}$$

Note that, in practice, the SFB and AFB should be efficiently implemented using the combination of an FFT and a polyphase network [16]. Commonly, in the FBMC literature, the channel is assumed to remain constant over the transmit and receive pulse duration and the channel is assumed to be frequency flat at the subcarrier level. Under these assumptions, we approximate the demodulated symbols $\mathbf{z}_{m,l}$ as

$$\mathbf{z}_{m,l} \approx e^{\jmath\phi_l}\mathbf{H}_m\left(\mathbf{d}_{m,l} + \jmath\mathbf{u}_{m,l}\right) + \mathbf{w}_{m,l},$$

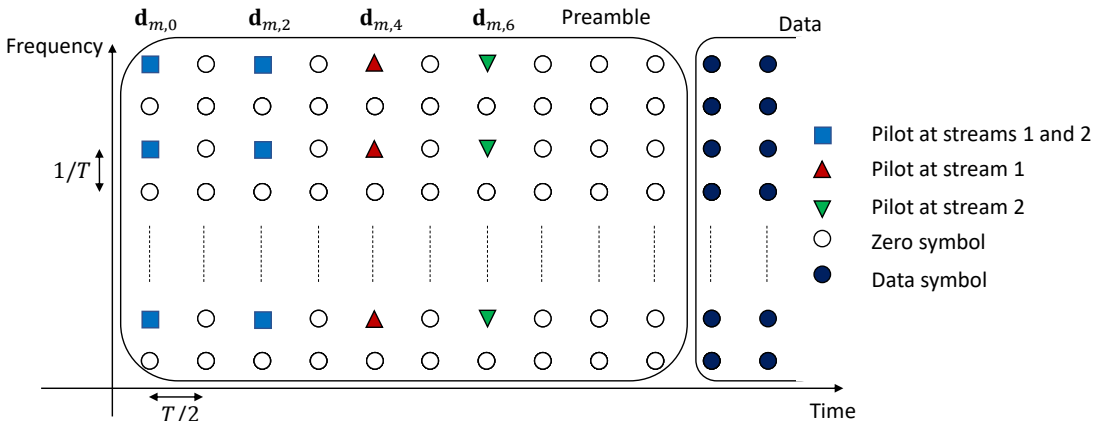


Fig. 2. Preamble structure for $S = 2$.

where $\mathbf{w}_{m,l}$ is additive noise and $\jmath\mathbf{u}_{m,l}$ is the purely imaginary so-called intrinsic interference coming from neighboring symbols in time and frequency. The MIMO matrix $\mathbf{H}_m \in \mathbb{C}^{S\times S}$ corresponds to the channel frequency response, assumed to be static over the frame duration. The phase $\phi_l$, which varies over time but not frequency, stands for the effect of phase noise and possible residual carrier frequency offset (CFO) after demodulation. The estimated real symbols $\hat{\mathbf{d}}_{m,l}$ are obtained by taking the real part, after channel equalization and phase compensation, i.e.,

$$\hat{\mathbf{d}}_{m,l} = \Re\left\{e^{-\jmath\hat{\phi}_l}\mathbf{B}_m\mathbf{z}_{m,l}\right\}.$$

The phase $\hat{\phi}_l$ is the estimate of $\phi_l$ while $\mathbf{B}_m$ is the estimate of the inverse of the channel $\mathbf{H}_m^{-1}$. Finally, the estimated complex symbols $\hat{\mathbf{c}}_{m,l}$ are obtained by real-to-complex conversion, i.e., the reciprocal part to the one at the transmitter. The next subsections will detail the algorithms that were used to synchronize the system, estimate the channel $\mathbf{H}_m$ and track the phase $\phi_l$.

### *2.1. Preamble structure*

The preamble structure that was used is shown in Fig. 2 in the particular case $S = 2$. It is made of the $6{+}2S$ first OQAM symbols $\mathbf{d}_{m,l}$, which corresponds to a duration of $(6{+}2S)T/2 = 3T{+}ST$. The preamble is constructed in order to avoid the influence of the intrinsic interference. Therefore, the 1st, 3th, ... $(3{+}2S)$th odd OQAM symbols are only zeros, i.e., $\mathbf{d}_{m,1} = \mathbf{d}_{m,3} = ... = \mathbf{d}_{m,3+2S} = \mathbf{0}\ \forall m$. Further, only even subcarriers are filled with pilots while the symbols on odd subcarriers are all zeros. Finally, to avoid influence from the data tones, an additional guard time of two OQAM symbols is added, i.e., $\mathbf{d}_{m,4+2S} = \mathbf{d}_{m,5+2S} = \mathbf{0}\ \forall m$.

The even subcarriers of the 0th OQAM symbol $\mathbf{d}_{m,0}$ are modulated with pseudo-randomly generated $\pm 1$, which prevents from increasing the peak-to-average power ratio of the preamble as would be the case for interference approximation methods [17]. For synchronization purposes, the 2nd OQAM symbol is a repetition of the first symbol, giving

$$\mathbf{d}_{m,0} = \mathbf{d}_{m,2} = \begin{cases} \begin{pmatrix}\pm 1\\ \pm 1\end{pmatrix} & \text{if } m \text{ is even and } m \in \mathcal{M} \\ \mathbf{0} & \text{if } m \text{ is odd or } m \notin \mathcal{M} \end{cases}.$$

For estimation purposes, the $(2{+}2s)$th symbol ($s = 1, 2, ..., S$) is only used to estimate the channel of the $s$th stream. Hence, at the $(2+2s)$th symbol, no pilots are transmitted on the $S-1$ streams

different from $s$, leading to

$$\mathbf{d}_{m,2+2s} = \begin{cases} \pm 1 \mathbf{e}_s & \text{if } m \text{ is even and } m \in \mathcal{M} \\ \mathbf{0} & \text{if } m \text{ is odd or } m \notin \mathcal{M} \end{cases},$$

where $\mathbf{e}_s$ is an all zero vector with a single one at the $s$th row. To simplify the notations in the following, we will denote by $\mathcal{M}_p$ the set of pilot subcarriers, i.e., all even subcarriers that belong to $\mathcal{M}$.

### *2.2. Synchronization*

The synchronization algorithm utilizes the repetitive pattern of the 0th and the 2nd symbols. It can be seen as a straightforward extension of the work in [18] to the MIMO case. The algorithms work in the frequency domain, which makes the algorithms very flexible. Thanks to high spectral containment of the prototype filter, it allows for instance not to take into account some parts of the spectrum in the presence of interferers or handling asynchronous users. In that case, these subcarriers can be simply discarded from the set $\mathcal{M}_p$.

The first step of the algorithm is to detect the start of the frame. This is done by maximizing the following detection metric computed based on the AFB outputs of the two receiving antennas,

$$\xi[l] = \frac{2\left|\sum_{m\in\mathcal{M}_p} \mathbf{z}_{m,l+2}^H \mathbf{z}_{m,l}\right|}{\sum_{m\in\mathcal{M}_p} \left(\|\mathbf{z}_{m,l}\|^2 + \|\mathbf{z}_{m,l+2}\|^2\right)}.$$

Once the beginning of the frame $l$ is detected, a first coarse CFO can be estimated by

$$\epsilon_{\text{CFO}} = \frac{1}{2\pi T} \angle \sum_{m\in\mathcal{M}_p} \mathbf{z}_{m,0}^H \mathbf{z}_{m,2}, \tag{2}$$

where the 0th OQAM symbol corresponds to the first demodulated symbol of the frame. Based on the coarse CFO estimate, the CFO can be corrected in the time domain before performing a second AFB demodulation. The CFO is then re-estimated using (2) again. The symbol timing offset (STO) is then estimated as

$$\tau_{\text{STO}} = \frac{T}{4\pi} \angle \sum_{i=\{1,2\}} \sum_{l=\{0,2\}} \sum_{\{m,m+2\}\in\mathcal{M}_p} \frac{z_{m+2,l}^{(i)*} z_{m,l}^{(i)}}{z_{m+2,l}^{(i)} z_{m,l}^{(i)}}.$$

The rest of the frame is demodulated using the refined CFO and STO estimates.

### *2.3. Channel estimation*

The channel estimation relies on the transmission of the $(2+2s)$th OQAM symbols ($s = 1, 2, ..., S$). Let us define the three following matrices

$$\begin{aligned} \mathbf{Z}_m &= \begin{pmatrix} \mathbf{z}_{m,4} & \mathbf{z}_{m,6} & \dots & \mathbf{z}_{m,2+2S} \end{pmatrix} \in \mathbb{C}^{S\times S} \\ \mathbf{W}_m &= \begin{pmatrix} \mathbf{w}_{m,4} & \mathbf{w}_{m,6} & \dots & \mathbf{w}_{m,2+2S} \end{pmatrix} \in \mathbb{C}^{S\times S} \\ \mathbf{D}_m &= \begin{pmatrix} \mathbf{d}_{m,4} & \mathbf{d}_{m,6} & \dots & \mathbf{d}_{m,2+2S} \end{pmatrix} \in \mathbb{C}^{S\times S}. \end{aligned}$$

Using the fact that, at the pilot positions, the intrinsic interference can be neglected thanks to the neighboring guard symbols ($\mathbf{u}_{m,l} \approx \mathbf{0}$) and assuming that the phase $\phi_l$ has not changed too much from the 4th to the $(2+2S)$th symbol, we can write

$$\mathbf{Z}_m = \mathbf{H}_m \mathbf{D}_m + \mathbf{W}_m,$$

and the least squares estimate of $\mathbf{H}_m$ at the pilot positions is simply given by $\hat{\mathbf{H}}_m = \mathbf{Z}_m \mathbf{D}_m^{-1}$. This operation is very simple since $\mathbf{D}_m$ is diagonal. Note that, in theory, $\mathbf{D}_m$ is not required to

be diagonal, meaning that multiple streams could be sending a pilot at the same time-frequency ressource. Other interesting designs use unitary matrices or Fourier matrices.

Still, the channel frequency response is only known at the pilot positions and the response at the non-pilot subcarriers should be interpolated. A straightforward interpolation can be done in the frequency domain by estimating the response at the non pilot subcarriers by an average of the response at the two neighboring pilot subcarriers. Another interpolation method can be conducted in the time domain. This method mainly assumes that the channel impulse response has an *a priori* known finite length $L$ and use it to average the noise effect [19]. The specific time domain method used here is detailed in [12]. In the experiments, we will compare the frequency and time domain methods.

### *2.4. Phase tracking*

The demodulated symbols can be affected by a phase rotation, which needs to be compensated for in order to avoid a phase drift. To track the phase $\phi_l$, we use the maximum a posteriori phase estimator derived in [13], which was straightforwardly extended to the MIMO case by combining not only all subcarriers but also the different streams of symbols. The algorithm proposed in [13] has a low complexity and is decision directed, which has the advantage of not requiring the insertion of pilots in the data frame and thus not decreasing the spectral efficiency.

The phase estimate at OQAM symbol $l$ is given by

$$\hat{\phi}_l = \hat{\phi}_{l-1} + \frac{(N_0+1)\sum_{m\in\mathcal{M}_p}\left(\tilde{\mathbf{z}}^I_{m,l}\right)^T \mathbf{d}_{m,l} - \sum_{m\in\mathcal{M}_p}\left(\tilde{\mathbf{z}}^R_{m,l}\right)^T \tilde{\mathbf{z}}^I_{m,l}}{\sum_{m\in\mathcal{M}_p}\left(\tilde{\mathbf{z}}^I_{m,l}\right)^T \tilde{\mathbf{z}}^I_{m,l} + \sigma^2_{\mathrm{MAP}}},$$

where $N_0$ is the noise variance. The symbols $\tilde{\mathbf{z}}^R_{m,l}$ and $\tilde{\mathbf{z}}^I_{m,l}$ are the real and imaginary part of the demodulated symbols after channel equalization and phase compensation relying on the previous estimate, i.e., $\tilde{\mathbf{z}}^R_{m,l} = \Re\left(e^{-\jmath\hat{\phi}_{l-1}}\mathbf{B}_m\mathbf{z}_{m,l}\right)$ and $\tilde{\mathbf{z}}^I_{m,l} = \Im\left(e^{-\jmath\hat{\phi}_{l-1}}\mathbf{B}_m\mathbf{z}_{m,l}\right)$. The estimated transmitted symbols $\mathbf{d}_{m,l}$ are obtained by direct detection on the symbols $\tilde{\mathbf{z}}^R_{m,l}$. Finally, the parameter $\sigma^2_{\mathrm{MAP}}$ is equal to $\sigma^2_{\mathrm{MAP}} = \frac{N_0}{2}(\frac{N_0}{2}+1)/\sigma^2_\epsilon$ with $\sigma^2_\epsilon$ defining how fast phase noise is varying.

## 3. Experimental Setup

The transceiver design proposed in Section 2 is experimentally validated in a 2x2 MIMO FBMC-OQAM signal over a seamless fiber–wireless in the W-band.

The DL experimental setup is shown in Fig. 3(a). The 2x2 MIMO FBMC signals are generated offline in Matlab, upconverted to 5 GHz and downloaded to two synchronized Arbitrary Waveform Generators (AWGs). At the centre station (CS), two optical signals with a frequency difference of 50 GHz from two different laser diodes (LDs) are modulated independently by the generated FBMC signals at Mach-Zehnder modulators (MZMs). The modulated optical signals are combined by an optical coupler (OC) and inputted into an optical attenuator (ATT) to adjust the transmit power. The signals are then amplified by an optical amplifier (EDFA) and transmitted to a RAU via a 20-km single-mode fiber (SMF). The received optical signals are separated into two branches by a 3-dB OC. At each branch, the optical signals are filtered by optical bandpass filters (OBPFs) to recover the transmitted modulated optical signals. After being converted to electrical formats by photo-detectors (PDs), the recovered signals at the intermediate frequency are up-converted to 81 GHz using electronic balanced mixers and local oscillators (LOs). In our experiment, for the sake of simplicity, the LO signals are generated by synthesizers and frequency up-converters at the RAU. However, to simplify the RAU, these LO signals can be delivered remotely from the CS using photonic technologies for generating and transmitting the LO signals [9]. The up-converted signals in the W-band are amplified by power amplifiers (PAs) before being emitted into free space by two 23-dBi horn antennas. After being transmitted over a 1-m free-space link, the signals are received by another two horn antennas at the remote radio head (RRH). The received signals are amplified by low-noise amplifiers (LNAs) in the W-band, and down-converted to the original

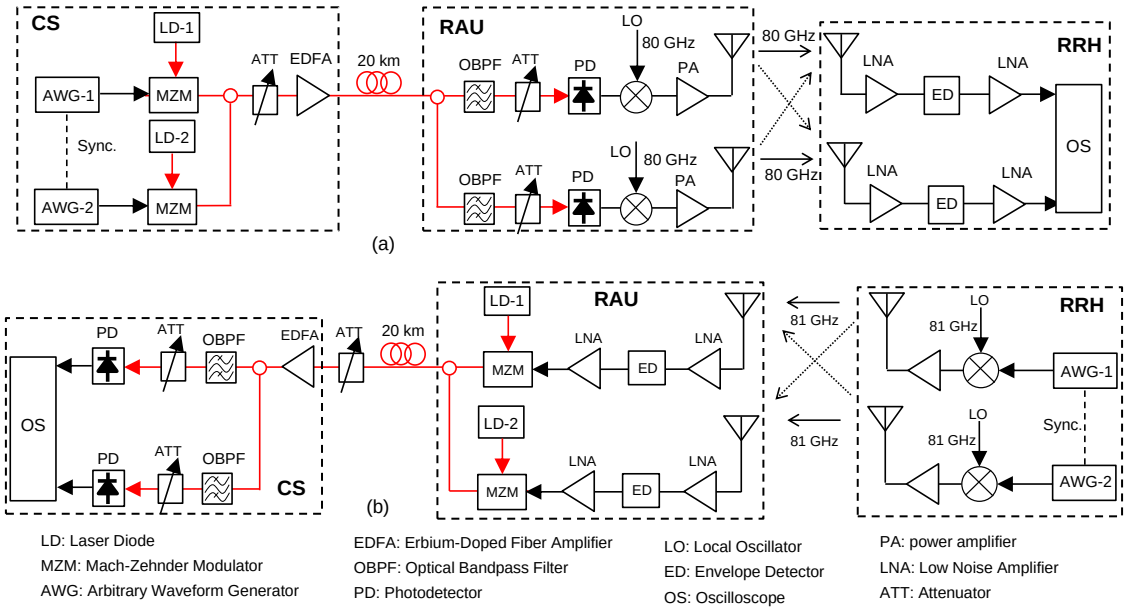


Fig. 3. Experimental setup.

signals by envelope detectors (EDs). The recovered signals are then amplified by LNAs in the microwave band and connected to a real-time oscilloscope (OS). Finally, the signals are sent to a personal computer and demodulated offline in Matlab.

The UL experimental setup is shown in Fig. 3(b). Similar to the DL direction, 2x2 MIMO FBMC signals are generated offline in Matlab, upconverted to 4.3 GHz and downloaded to two AWGs. All parameters of the signals are the same as in the downlink direction. The generated FBMC signals are up-converted to the W-band using two electrical balanced mixers and LO sources. The up-converted signals are amplified by PAs before being transmitted into free space by horn antennas. The signals are transmitted over the same 1-m free-space link as in the DL, and received by two horn antennas at the RAU. The signals are then amplified by LNAs before being coupled into two EDs for down-converting to the originally transmitted FBMC signals. The signals are then amplified by LNAs in the microwave band before modulating optical signals from two different LDs at two MZMs for conversion to optical signals. The modulated optical signals are combined by a 3-dB OC and transmitted to the CS by a 20-km SMF as in the DL. At the CS, the optical signals are amplified by an EDFA and separated into two branches by a 3-dB OC. The optical signal in each branch is then inputted to an OBPF to recover the transmitted optical signals. The received optical signals are converted to the original 2x2 MIMO FBMC signals by two PDs. Finally, the recovered signals are connected to the real-time OS and demodulated offline in Matlab.

In the experiment, to demonstrate a scalable system that can be applied for the signal transmission over a large-scale MIMO fiber–wireless system, we use a WDM IFoF system for optical links. Different electrical LO signal sources are also used for the signal up-conversion at the RAU. One should note that this system demonstration meets the general assumptions that were made in Section 2 on the channel variations in the time and frequency domains. Indeed, the link is relatively static and does not change fast over time, except for relatively slow changes due to phase noise. In our system, the two electrical LOs used for signal up-conversion to W-band are synchronized. However, there is still some difference in the phases of the oscillators, resulting in the presence of phase noise. Further, since the optical link is made of a few tens of kilometers and the system bandwidth is of the order of the GHz, the dispersion effect of the fiber remains quite limited. Furthermore, the millimeter-wave link is mainly composed of line-of-sight components and

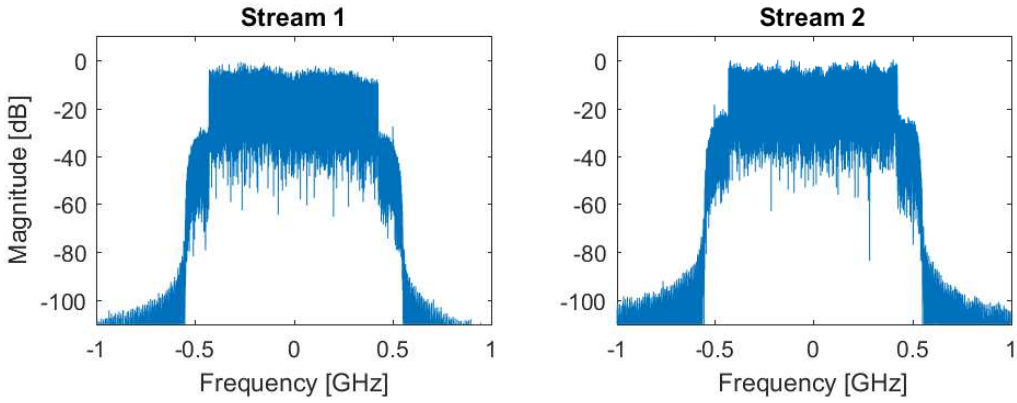


Fig. 4. Downlink received baseband spectrum of received signals at antennas 1 and 2, $1/T_s = 1000$ MBd.

does not suffer much from multipath fading, resulting in slow variations of the channel in frequency, as will be further demonstrated in the next section.

Because of the space limitation of the setup, the length of the 80-GHz wireless link was limited to 1 meter. To avoid nonlinear distortion of the EDs, the received optical power at the input of the PDs in the DL direction were limited to approximately -3 dBm. In addition, the power of the LO signals at the input of the electrical mixers was limited to 6 dBm. In the UL direction, the AWGs power at the input of the mixers was also adjusted by electrical variable attenuators. The transmit power of the 80 GHz wireless link was approximately 0 dBm (before the transmit antennas). Further increase in the transmission power can help increase the wireless link transmission range. In our previous work [20], we confirmed that a transmission distance of hundred meters to a kilometer could be achieved using high-gain antennas and high-output PAs. In this kind of highly directive wireless links, the effects of multipath fading can be neglected.

## 4. Experimental Results

This section aims at demonstrating and evaluating the performance of the 2x2 MIMO FBMC-OQAM fiber–wireless system using the proposed transceiver design. For the experiments, different simulation parameters are considered. The number of subcarriers is fixed to 512, if not stated otherwise. Out of all subcarriers, 5% on each edge of the spectrum are left inactive. The prototype filter is the Phydyas pulse [15] with overlapping factor $\kappa = 4$. The constellation is 16-QAM. Five values of the Baud rate are considered for the system, i.e., $1/T_s = 500$ MBd, $1/T_s = 1000$ MBd, $1/T_s = 1600$ MBd, $1/T_s = 2000$ MBd and $1/T_s = 2500$ MBd. The total bit rate can then be computed as

$$\mathrm{R} = \overbrace{2}^{\text{Number of streams}} \times \underbrace{4}_{\text{16-QAM}} \overbrace{\lfloor 0.9M \rfloor}^{\text{Active subcarriers}} \underbrace{\frac{1}{MT_s}}_{\text{Inverse of symbol period}} \quad \text{[bps]}.$$

In numbers, this gives $3.6$, $7.2$, $11.6$, $14.4$ and $18$ Gb/s for the $500$, $1000$, $1600$, $2000$ and $2500$ MBd systems respectively. The downlink received baseband spectrum of received signals at antennas 1 and 2 are shown in Fig. 4. The polarization of the transmit and receive antennas can be chosen to be the same or different between each stream, to avoid inter-antenna interference. The error vector magnitude (EVM), expressed in %, is used as the main figure of merit and is defined as

$$\mathrm{EVM} = 100\sqrt{\mathbb{E}\|\hat{\mathbf{d}}_{m,l} - \mathbf{d}_{m,l}\|^2} \quad [\%].$$

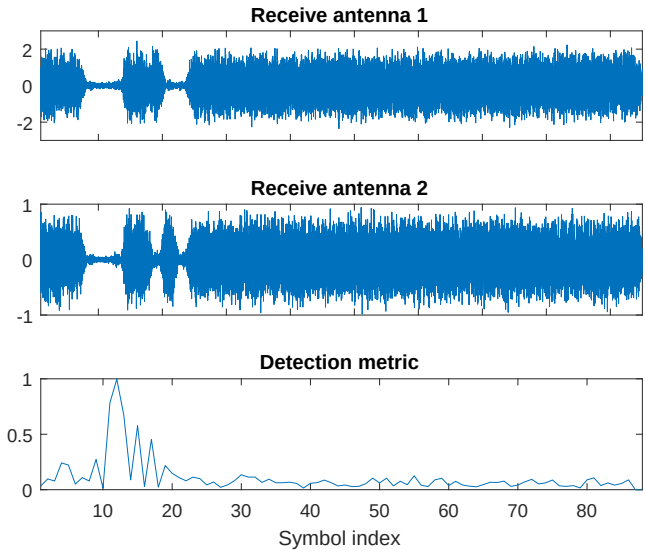


Fig. 5. Baseband received signals and detection metric for antennas with different polarization in downlink and $1/T_s = 1000$ MBd.

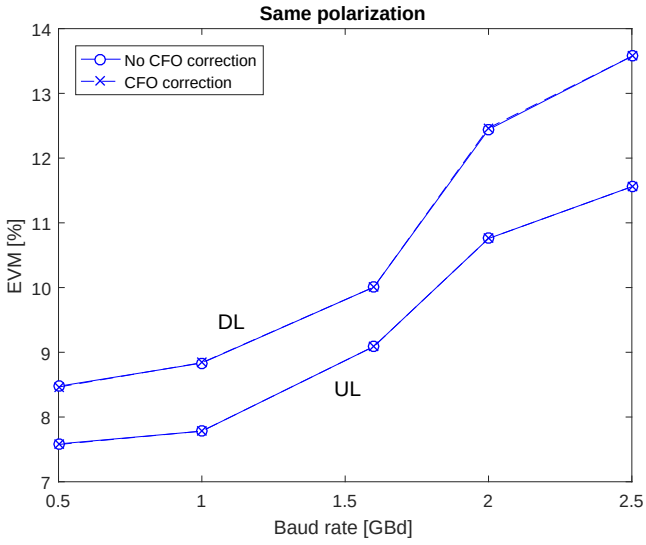


Fig. 6. The system performance with and without using CFO compensation.

### *4.1. Synchronization*

In Fig. 5, the magnitudes of the received baseband signals for the two streams are plotted after downconversion to baseband. The AWGs were generating the same frame periodically. The preamble section of the frame can be clearly identified. The detection metric detailed previously using the signals of the two receiving antennas leads to a sharp peak to jointly estimate the start of the frame. Note that the two smaller following peaks are due to the following pilot symbols aimed at channel estimation, as was shown in the preamble structure in Fig. 2.

Fig. 6 plots the EVM in DL and UL directions by switching on or off the CFO correction. As can be seen, the performance is similar and hence, we see that the system is not sensitive to CFO. This makes sense since the receiver is non coherent and that the electrical oscillators at the RAU are synchronized, as explained in Section 3. Therefore, the system does not require the

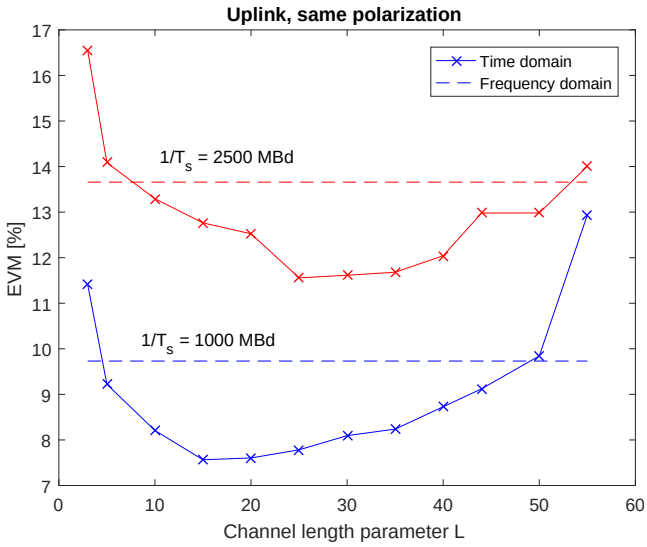


Fig. 7. Time domain versus frequency domain channel estimation and $1/T_s = 1000$ MBd.

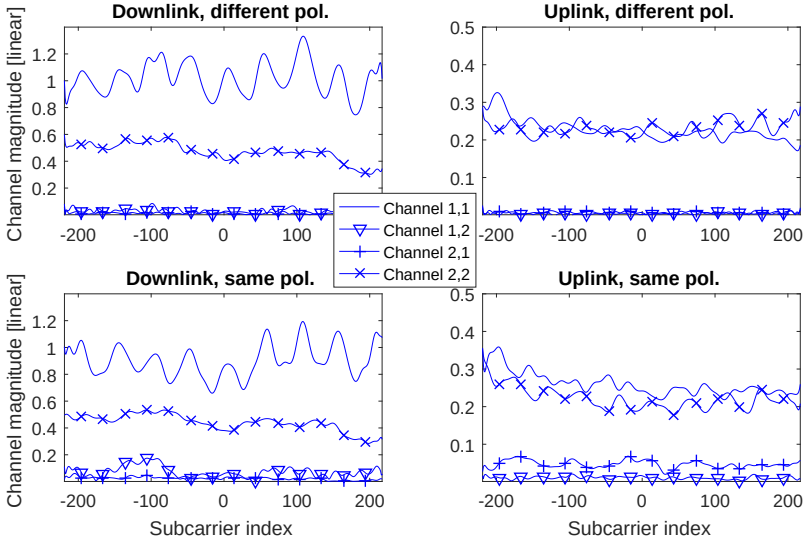


Fig. 8. Channel frequency response between each pair of transmitted and received streams and $1/T_s = 1000$ MBd.

CFO correction algorithm, which simplifies the receiver implementation.

### *4.2. Channel estimation*

In Fig. 7, the EVM of the uplink system is plotted for the two channel estimation interpolation methods and for two different Baud rates.

The horizontal axis of Fig. 7 corresponds to the channel impulse response length $L$, which needs to be fixed for the time domain interpolation method. The EVM reaches a minimum for a particular value of $L$. Indeed, for too small values, missing taps of the channel are not estimated while for too large values, more taps than the actual channel length are estimated, resulting in a larger sensitivity to noise. One can note that the minimum value of the EVM for the 2500 MBd system corresponds to an approximately 2.5 times larger value of $L$ than for the 1000 MBd. This makes sense since the sampling frequency $1/T_s$ is 2.5 higher. On the other hand, the frequency

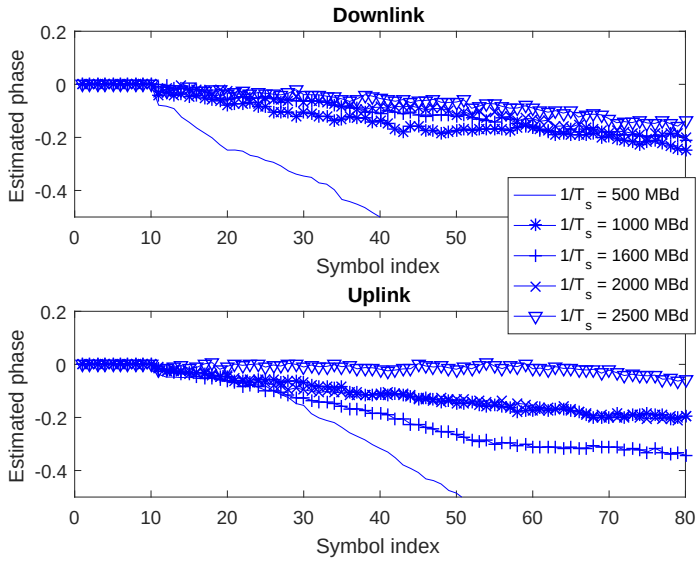


Fig. 9. Evolution of the estimated phase as a function of time (same polarization). One realization of the phase is plotted for each Baud rate.

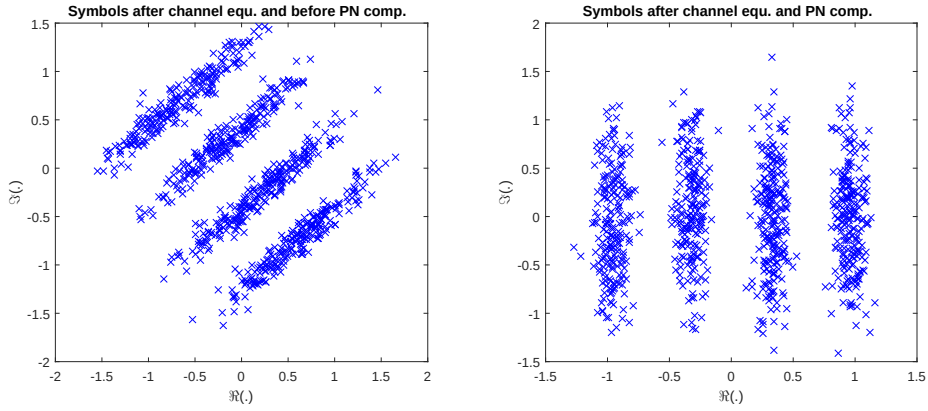


Fig. 10. Constellation plot of the demodulated symbols at one multicarrier symbol after channel equalization and before/after PN compensation for same antenna polarization, DL and $1/T_s = 500$ MBd.

domain method does not depend on any parameter. For most values of $L$, the time domain method is more performant than the frequency domain method. The gain comes from the averaging of the noise. Indeed, all pilot subcarriers outputs are combined to jointly estimate the time domain coefficients. In the following simulations, the time domain interpolation method was used with the parameter $L$ fixed to the value of 25.

Fig. 8 plots the channel frequency response evaluated at each active subcarrier and for each pair of streams. As can be seen in the upper subfigures, when the polarization of the antennas is different for each stream, there is almost no inter-stream interference while it is stronger for the same polarization. An interesting observation is to see that one interfering channel is almost null. This can be explained by the position of the antennas and their quite directive pattern.

### *4.3. Phase tracking*

In our system, even though EDs are used for the signal down-conversion at the RRHs, some phase noise is observed in the received signals. This is due to the fact that when the antennas

are placed closed each other, the LO signal component, which is much larger than the mixed sideband signals, from one transmit antenna will leak to the other receive antenna and vice versus. As a result, the LO signal components of the input signal to the EDs at RRHs are the sum of the corresponding LO signal from the transmit antenna and the leaked LO signal from the other transmit antenna. Because the frequency of the LOs are same, the LO signals will be added up and the phase of the LO signal component to each ED is the summed phases from different LOs. This explains why the PN compensation is still needed in our system. We should note that when one common LO signal is used for the MIMO signal up-conversion to many antennas, the observed PN drift might not exist. However, for a large-scale MIMO system, the use of multiple LO signal sources are necessary due to the limited output power from one single LO signal generator.

Fig. 9 shows the estimated phase as a function of the symbol in time for different system Baud rates. In Fig. 10, the constellation of the symbols $\tilde{z}_{m,l}$ are plotted and refer to the demodulated symbols after channel equalization and before/after PN compensation, i.e., $\mathbf{B}_m\mathbf{z}_{m,l}$ and $e^{-\jmath\hat{\phi}_l}\mathbf{B}_m\mathbf{z}_{m,l}$. In the OQAM modulations, the QAM symbols are mapped to PAM purely real symbols and so a complex 16-QAM constellation is mapped to two real 4-PAM constellations. As explained in Section 2, after demodulation, if the channel and PN are perfectly compensated for, we should retrieve the purely real transmitted symbols impacted by purely imaginary intrinsic interference, *i.e.*, $\mathbf{d}_{m,l} + \jmath\mathbf{u}_{m,l}$. This is what we see in the right figure of Fig. 10. On the real axis, we can retrieve the four possible values for the real transmitted symbols (4-PAM) while on the imaginary axis, the intrinsic interference is approximately normally distributed around zero.

Clearly, Fig. 9 and 10 show that a phase drift is present and it induces a rotation of the symbols before the real conversion (see Fig.1). This phase rotation needs to be compensated for before real conversion to avoid leakage of the intrinsic interference on the purely real transmitted symbol. Furthermore, we can see in the right figure that the PN compensation algorithm succeeds in correcting the phase drift so that the purely imaginary intrinsic interference will be completely removed after real conversion.

### *4.4. Comparison with OFDM*

The downlink OFDM received baseband spectrum of received signals at antennas 1 and 2 are shown in Fig. 11. Fig. 12 plots the downlink EVM of each stream as a function of the system Baud rate for FBMC and OFDM modulations and 512 subcarriers. For the OFDM modulation, a similar frame structure was considered with a preamble designed for synchronization and channel estimation. The cyclic prefix was fixed to one fourth of the symbol period. This implies that the FBMC throughput is 25% higher than the OFDM one, as shown in Table I. As one can see, the two modulations perform similarly in terms of EVM. The performance slightly degrades as the Baud

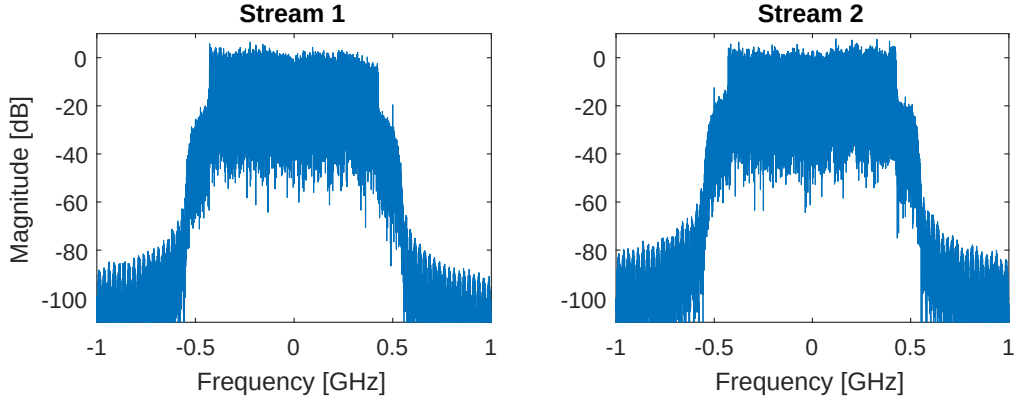


Fig. 11. Downlink OFDM received baseband spectrum of received signals at antennas 1 and 2, $1/T_s = 1000$ MBd.

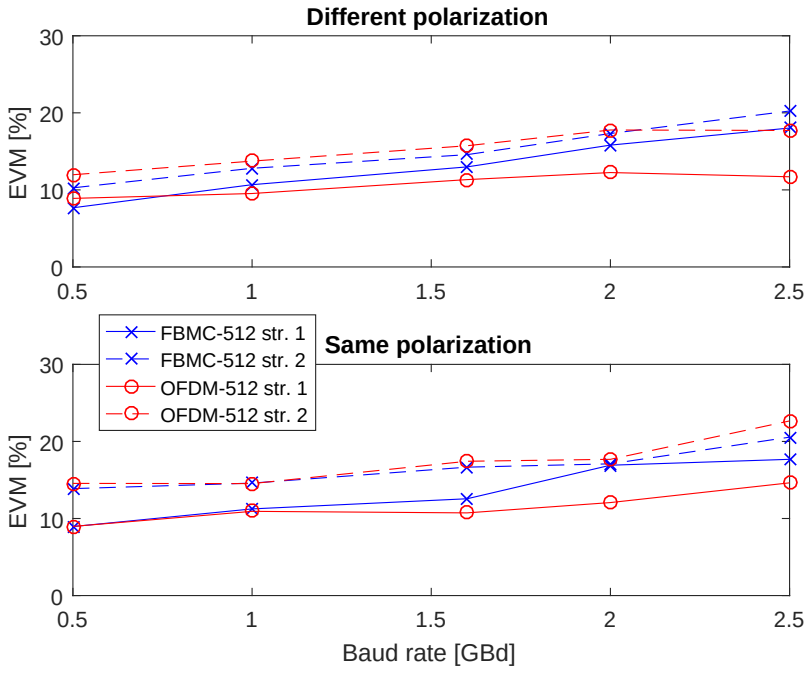


Fig. 12. Downlink EVM of each stream as a function of the system rate for FBMC and OFDM modulations and 512 subcarriers.

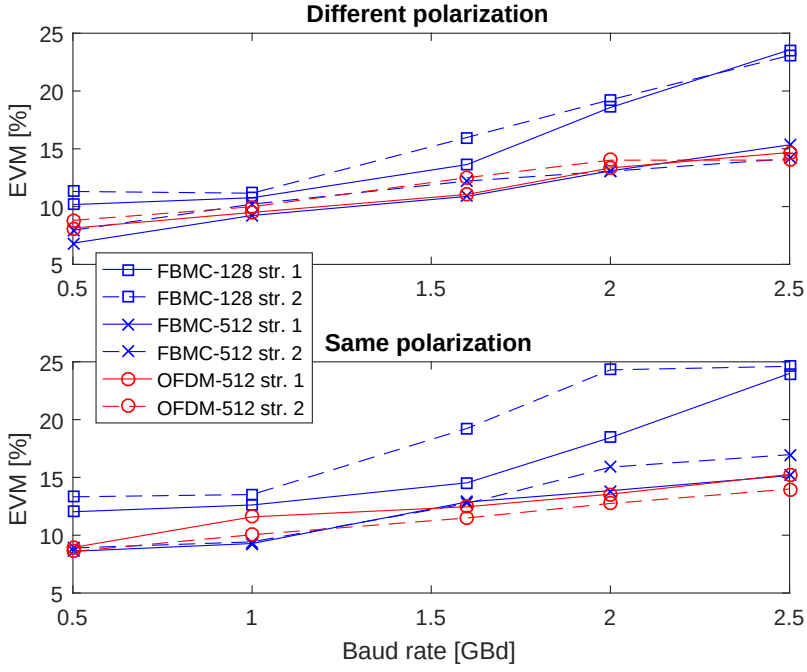


Fig. 13. Uplink EVM of each stream as a function of the system rate for FBMC and OFDM modulations and 512/128 subcarriers.

rate increases. As could be expected from Fig. 8, stream 1 has a relatively better performance since its channel frequency response is stronger.

Fig. 13 plots the corresponding figure as Fig. 12 in the uplink with the additional performance

TABLE I
THROUGHPUT COMPARISON BETWEEN FBMC-OQAM AND CP-OFDM SYSTEMS.

| Baud rate $1/T_s$ | FBMC-OQAM bit rate | CP-OFDM bit rate |
|---|---|---|
| 500 MBd | 3.6 Gb/s | 2.9 Gb/s |
| 1000 MBd | 7.2 Gb/s | 5.8 Gb/s |
| 1600 MBd | 11.6 Gb/s | 9.2 Gb/s |
| 2000 MBd | 14.4 Gb/s | 11.5 Gb/s |
| 2500 MBd | 18 Gb/s | 14.4 Gb/s |

of a FBMC system having 128 subcarriers. OFDM and FBMC again perform similarly for 512 subcarriers. The FBMC performance is degraded for the lower number of subcarriers 128. This can be explained by the fact that the channel becomes relatively more selective in frequency. In this case, the channel estimation and equalization algorithms become less efficient. From this observation, an optimal number of subcarriers should be chosen to optimize the system performance.

## 5. Conclusions

In this paper, we proposed a general framework for MIMO FBMC-OQAM transmission systems, including the description of algorithms for mitigation of the channel impairments. The proposed system is scalable in the number of transmitted streams and flexible as multiple asynchronous users can be accommodated. The transceiver chain is experimentally validated in a 2x2 MIMO FBMC-OQAM signal over a seamless fiber–wireless in the W-band. The system uses a high spectral efficiency WDM IFoF for MIMO signal transmission in the optical links, and an electrical up-conversion at the RAU. Satisfactory performance is confirmed for a data rate of up to 18 Gb/s in both DL and UL directions. We also observed that even though a simple intensity modulation and direct detection method is used, there is some phase drift in the received signals when multiple LO signal sources are used. This is due to the leakage of the local oscillators and the difference in the phase variations of the LOs. Our proposed system can be very useful for high spectral efficiency seamless fiber–wireless mobile fronthaul system and/or for transmission of large-scale MIMO mobile signals in the high frequency bands over a fiber optic fronthaul system.

## References


[1] X. Pang, A. Caballero, A. Dogadaev, V. Arlunno, R. Borkowski, J. S. Pedersen, L. Deng, F. Karinou, F. Roubeau, D. Zibar, X. Yu, and I. T. Monroy, "100 Gbit/s hybrid optical fiber-wireless link in the W-band (75–110 GHz)," *Opt. Express*, vol. 19, no. 25, pp. 24 944–24 949, Dec 2011. [Online]. Available: http://www.opticsexpress.org/abstract.cfm?URI=oe-19-25-24944

[2] X. Li, J. Yu, and J. Xiao, "Demonstration of Ultra-Capacity Wireless Signal Delivery at W-Band," *Journal of Lightwave Technology*, vol. 34, no. 1, pp. 180–187, Jan 2016.

[3] P. T. Dat, A. Kanno, N. Yamamoto, and T. Kawanishi, "Full-Duplex Transmission of LTE-A Carrier Aggregation Signal Over a Bidirectional Seamless Fiber-Millimeter-Wave System," *Journal of Lightwave Technology*, vol. 34, no. 2, pp. 691–700, Jan 2016.

[4] S. E. Alavi, I. S. Amiri, M. Khalily, N. Fisal, A. S. M. Supa'at, H. Ahmad, and S. M. Idrus, "W-Band OFDM for Radio-over-Fiber Direct-Detection Link Enabled by Frequency Nonupling Optical Up-Conversion," *IEEE Photonics Journal*, vol. 6, no. 6, pp. 1–7, Dec 2014.

[5] L. Deng, X. Pang, Y. Zhao, M. B. Othman, J. B. Jensen, D. Zibar, X. Yu, D. Liu, and I. T. Monroy, "2x2 MIMO-OFDM Gigabit fiber-wireless access system based on polarization division multiplexed WDM-PON," *Opt. Express*, vol. 20, no. 4, pp. 4369–4375, Feb 2012. [Online]. Available: http://www.opticsexpress.org/abstract.cfm?URI=oe-20-4-4369

[6] B. Farhang-Boroujeny, "OFDM Versus Filter Bank Multicarrier," *IEEE Signal Processing Magazine*, vol. 28, no. 3, pp. 92–112, May 2011.

[7] M. Xu, J. Zhang, F. Lu, J. Wang, L. Cheng, H. J. Cho, M. I. Khalil, D. Guidotti, and G. K. Chang, "FBMC in Next-Generation Mobile Fronthaul Networks With Centralized Pre-Equalization," *IEEE Photonics Technology Letters*, vol. 28, no. 18, pp. 1912–1915, Sept 2016.

[8] J. Zhang, M. Xu, J. Wang, F. Lu, L. Cheng, H. Cho, K. Ying, J. Yu, and G. K. Chang, "Full-Duplex Quasi-Gapless

Carrier Aggregation Using FBMC in Centralized Radio-Over-Fiber Heterogeneous Networks," *Journal of Lightwave Technology*, vol. 35, no. 4, pp. 989–996, Feb 2017.

[9] P. T. Dat, A. Kanno, N. Yamamoto, and T. Kawanishi, "Simultaneous transmission of multi-RATs and mobile fronthaul in the MMW bands over an IFoF system," in *2017 Optical Fiber Communications Conference and Exhibition (OFC)*, March 2017, pp. 1–3.

[10] J. He, B. Li, L. Deng, M. Tang, L. Gan, S. Fu, P. P. Shum, and D. Liu, "Experimental investigation of inter-core crosstalk tolerance of MIMO-OFDM/OQAM radio over multicore fiber system," *Opt. Express*, vol. 24, no. 12, pp. 13 418–13 428, Jun 2016. [Online]. Available: http://www.opticsexpress.org/abstract.cfm?URI=oe-24-12-13418

[11] C. Liu, L. Deng, J. He, D. Li, S. Fu, M. Tang, M. Cheng, and D. Liu, "Experimental demonstration of high spectral efficient 4  4 MIMO SCMA-OFDM/OQAM radio over multi-core fiber system," *Opt. Express*, vol. 25, no. 15, pp. 18 431–18 441, Jul 2017. [Online]. Available: http://www.opticsexpress.org/abstract.cfm?URI=oe-25-15-18431

[12] F. Rottenberg, F. Horlin, E. Kofidis, and J. Louveaux, "Generalized optimal pilot allocation for channel estimation in multicarrier systems," in *2016 IEEE 17th International Workshop on Signal Processing Advances in Wireless Communications (SPAWC)*, July 2016, pp. 1–5.

[13] F. Rottenberg, T. H. Nguyen, S. P. Gorza, F. Horlin, and J. Louveaux, "ML and MAP phase noise estimators for optical fiber FBMC-OQAM systems," in *2017 IEEE International Conference on Communications (ICC)*, May 2017, pp. 1–6.

[14] P. Siohan, C. Siclet, and N. Lacaille, "Analysis and design of OFDM/OQAM systems based on filterbank theory," *IEEE Trans. Signal Process.*, vol. 50, no. 5, pp. 1170–1183, 2002.

[15] M. G. Bellanger, "Specification and design of a prototype filter for filter bank based multicarrier transmission," in *IEEE International Conference on Acoustics, Speech, and Signal Processing*, 2001, pp. 2417–2420.

[16] P. Siohan, C. Siclet, and N. Lacaille, "Analysis and design of OFDM/OQAM systems based on filterbank theory," *IEEE Transactions on Signal Processing*, vol. 50, no. 5, pp. 1170–1183, May 2002.

[17] E. Kofidis, D. Katselis, A. Rontogiannis, and S. Theodoridis, "Preamble-based channel estimation in OFDM/OQAM systems: A review," *Signal Process.*, vol. 93, no. 7, pp. 2038–2054, July 2013. [Online]. Available: http://dx.doi.org/10.1016/j.sigpro.2013.01.013

[18] C. Thein, M. Schellmann, and J. Peissig, "Analysis of frequency domain frame detection and synchronization in oqam-ofdm systems," *EURASIP Journal on Advances in Signal Processing*, vol. 2014, no. 1, p. 83, Jun 2014. [Online]. Available: https://doi.org/10.1186/1687-6180-2014-83

[19] M. K. Ozdemir and H. Arslan, "Channel estimation for wireless OFDM systems," *IEEE Communications Surveys Tutorials*, vol. 9, no. 2, pp. 18–48, Second 2007.

[20] A. Kanno, P. T. Dat, T. Kuri, I. Hosako, T. Kawanishi, Y. Yoshida, Y. Yasumura, and K. Kitayama, "Coherent Radio-Over-Fiber and Millimeter-Wave Radio Seamless Transmission System for Resilient Access Networks," *IEEE Photonics Journal*, vol. 4, no. 6, pp. 2196–2204, Dec 2012.